Preprint
UCRL-JC-137668

EUV Engineering Test Stand

D. A. Tichenor, G. D. Kubiak, W. C. Replogle, L. E. Klebanoff, J. B. Wronosky, L. C. Hale, H. N. Chapman, J. S. Taylor, J. A. Folta, C. Montcalm, and R. M. Hudyma

This article was submitted to
25th Annual International Symposium on Microlithography, Santa Clara, CA, February 27-March 3, 2000

February 14, 2000

EUV Engineering Test Stand

Daniel A. Tichenor*[a], Glenn D. Kubiak[a], William C. Replogle[a], Leonard E. Klebanoff[a], John B. Wronosky[b], Layton C. Hale[c], Henry N. Chapman[c], John S. Taylor[c], James A. Folta[c], Claude Montcalm[c], and Russell M. Hudyma[c]

[a]Sandia National Laboratories, PO Box 969, Livermore CA 94551
[b]Sandia National Laboratories, PO Box 5800, Albuquerque NM 87185
[c]Lawrence Livermore National Laboratory, PO Box 808, Livermore, CA 94550

ABSTRACT

The Engineering Test Stand (ETS) is an EUV laboratory lithography tool. The purpose of the ETS is to demonstrate EUV full-field imaging and provide data required to support production-tool development. The ETS is configured to separate the imaging system and stages from the illumination system. Environmental conditions can be controlled independently in the two modules to maximize EUV throughput and environmental control. A source of 13.4 nm radiation is provided by a laser plasma source in which a YAG laser beam is focused onto a xenon-cluster target. A condenser system, comprised of multilayer-coated mirrors and grazing-incidence mirrors, collects the EUV radiation and directs it onto a reflecting reticle. A four-mirror, ring-field optical system, having a numerical aperture of 0.1, projects a 4x-reduction image onto the wafer plane. This design corresponds to a resolution of 70nm at a k_1 of 0.52. The ETS is designed to produce full-field images in step-and-scan mode using vacuum-compatible, one-dimension-long-travel magnetically levitated stages for both reticle and wafer. Reticle protection is incorporated into the ETS design. This paper provides a system overview of the ETS design and specifications.

Keywords: EUVL, lithography, multilayers coatings, optical fabrication, optical design, laser-produced plasma, laser plasma source, maglev, magnetic levitation, stages, precision engineering

1. INTRODUCTION

Extreme Ultraviolet Lithography (EUVL) is one of the leading candidates for patterning semiconductor devices during the next decade. The development of multilayer coatings[1] for wavelengths between 11nm and 14 nm enables the design of all-reflecting systems that support multiple generations of microlithography technology, capable of feature sizes down to 30 nm. The development of EUVL technology is funded by the EUV, Limited Liability Company (LLC), a consortium of semiconductor manufacturers founded in 1997 and comprised of Advanced Micro Devices, Intel and Motorola. The Department of Energy Virtual National Laboratory, comprised of Lawrence Berkeley National Laboratory, Lawrence Livermore National Laboratory and Sandia National Laboratories, perform research, development, and engineering leading to the commercialization of EUVL. A major component of this effort is the development of the EUV Engineering Test Stand (ETS), an alpha-class tool designed to demonstrate full-field EUV imaging and provide data to participating equipment manufacturers to support production-tool development.

EUV images with resolution as high as 50 nm have been demonstrated using the 10x microstepper.[2] This tool, designed for proof-of-principle experiments, utilized a simple condenser, small-field projection system and low power EUV source. The ETS incorporates major advances in all subsystems including: a high-power laser-produced-plasma source, a large-solid-angle condenser, an advanced ring-field projection system, precision scanning stages and an advanced environmental system.

2. ETS DESIGN AND INTEGRATION

The major components of the ETS illuminator are the source, condensing optics, and environmental enclosure (see Fig. 1). The source of EUV radiation is provided by a laser-produced plasma generated by a YAG laser beam focused onto a xenon-cluster target. The collector, the first component in the condenser system, collects EUV radiation over a solid angle of 1.68 sterradians using six identical aspheric elements coated with Mo/Si multilayers that are optimized for reflection at 13.4 nm. The EUV beam collected in each of the six channels is shaped and directed by a grazing-incidence mirror and a near-normal mirror, located in the illuminator enclosure. A membrane-type spectral purity filter removes out-of-band radiation and

* Correspondence: Email: datiche@sandia.gov; Telephone: 925 294 2137; Fax: 925 294 3870

provides an environmental barrier between the illuminator and main enclosure. The six beams are combined and further conditioned by a final grazing-incidence element, C4, to illuminate at the reticle and to achieve an effective aperture fill factor of 0.7.

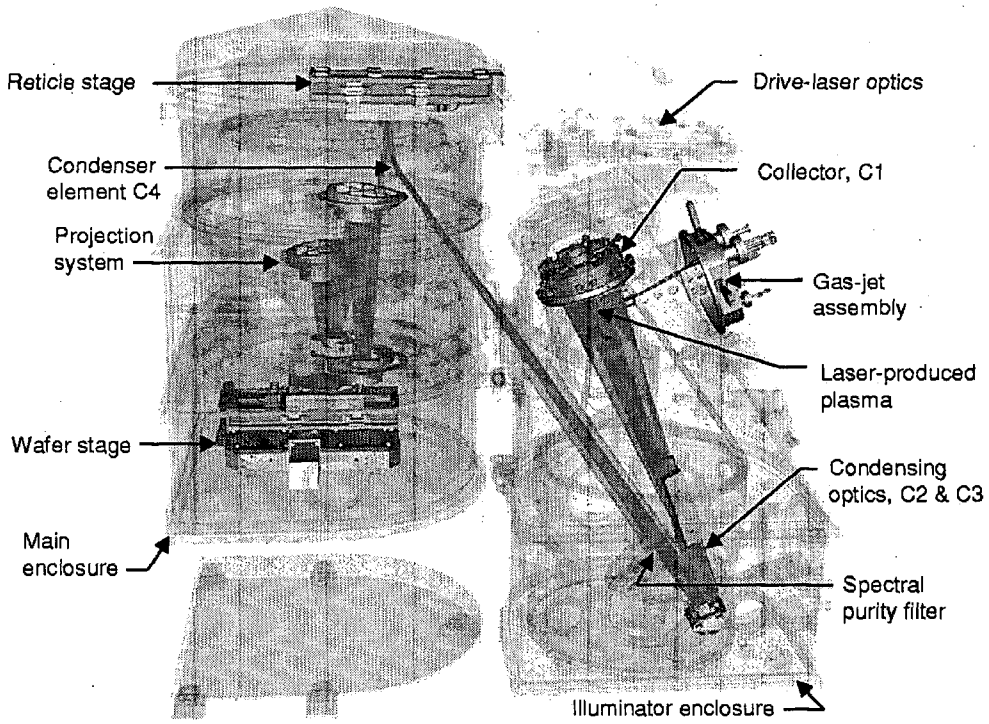

Figure 1. Solid model of the EUV Engineering Test Stand.

The ETS projection system, a four-mirror, ring-field design, projects an image of the reflecting reticle onto the wafer within a print field 1.5 mm wide by 24 mm long. The projection optics are designed to print 4x-reduction, full-field images in step-and-scan mode, using a numerical aperture of 0.1. The ETS design requirement for printing 100 nm features is satisfied by this optical design, which also supports the printing of 70 nm features at a k_1 of 0.52. The projection system is kinematically mounted on a rigid metrology frame of invar which is carried on a set of three active/passive isolators to protect it from ground vibrations.

The reticle and wafer are electrostatically clamped and carried on magnetically-levitated (maglev) stages, which are mounted on a grounded structure. This design assures that the reaction forces, resulting from stage acceleration, are shunted to ground without exciting modes in the projection system or support structures. Each stage controls 5 degrees of freedom over short travel ranges and one long-travel degree of freedom in the scanning direction. A laser metrology system feeds the positions of the wafer and reticle platens to a high-speed digital control system, designed to achieve precision scanning, while isolating the suspended reticle and wafer from ground vibrations induced in the stage bases.

The environmental enclosure is comprised of two primary components, the illuminator enclosure containing the source and condenser and the main enclosure containing the C4 condensing element, the projection optics box and the scanning stages. Within the main enclosure special seals create three separate zones: the reticle zone containing the reticle stage, the optics zone containing the projection optics and stage metrology, and the wafer zone containing the wafer stage. This configuration provides the flexibility to implement environmental conditions designed to protect the optics from carbon contamination due to cracking of hydrocarbons on the mirror surfaces and to protect the reticle from particulate contamination.

The top-level ETS specifications are summarized in Table 1.

Table 1. EUV Engineering Test Stand System Requirements	
EUV power at wafer	22.6 mw
Operating wavelength	13.4 nm
Wafer size	200 mm
Reduction ratio	4:1
Field size	24 x 32.5 mm scanned
Numerical aperture	0.1
Width of ring field	1.5 mm
Partial coherence	0.7
Illumination uniformity	±2%
Resolution (dense features) @ $k_1 = 0.52$	70 nm
Resolution (isolated features) @ $k_1 = 0.52$	50 nm
Critical dimension control within a field	15 nm 3 σ
Image distortion	11 nm total range
Depth of focus	±0.5 μm
Stage synchronization jitter	10 nm rms
Stage mean position error	±3 nm rms
Overlay (to be implemented in phase 2)	50 nm mean +3 σ

3. ILLUMINATOR SUBSYSTEM

There are three major components of the ETS illuminator as shown schematically in Fig. 2: a 1700 watt pulsed laser that drives the plasma, a gas jet system that provides a target of solid xenon particles, and a multi-element condenser that collects a large fraction of the emitted radiation and directs it onto the reticle.

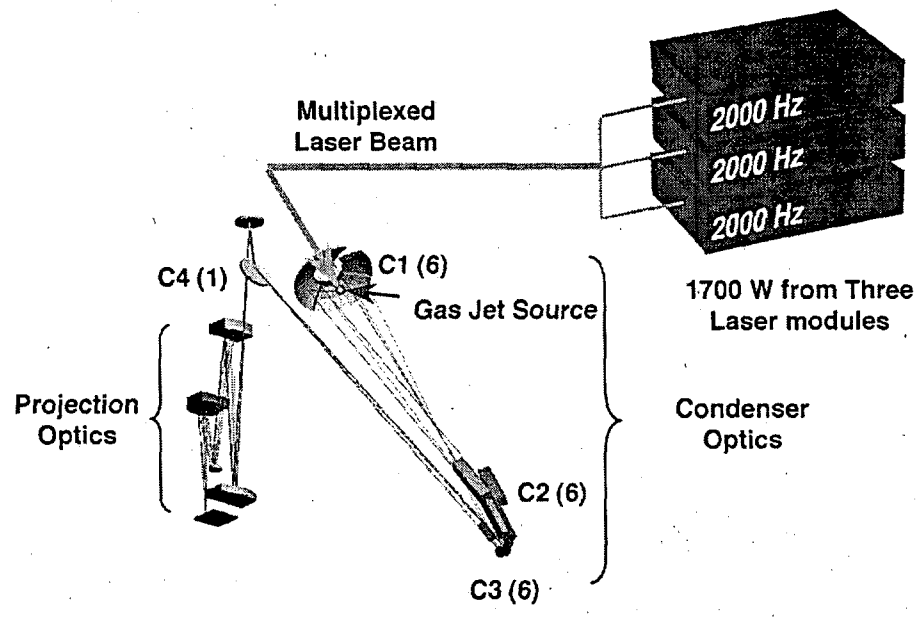

Figure 2. Schematic diagram of the high-power EUV laser plasma source and illumination system.

3.1 Source

The EUV illumination system requirements for the ETS exposure tool are tabulated in Table 2 and described in more detail in Ref. 3. To meet these requirements, a high-power jet source and illumination system has been developed. It consists of a gas jet target, 1700 W solid-state laser driver, and a large-solid-angle condenser, each of which will be described in turn. The target medium for the laser plasma source is supplied by a continuous gas jet system developed by Advanced Energy Systems and described in a previous publication.[4] The jet source produces a target stream of Xe clusters via supersonic expansion. Typical stagnation pressures are in the range from 10-15 bar. The nozzle is engineered to maximize the degree of Xe condensation for optimum EUV generation and also to minimize the attenuation of EUV by uncondensed Xe gas. An efficient pumping scheme is employed to reduce the ambient pressure of Xe to 1 mTorr under normal operation. To reduce recurring costs associated with Xe use, the system is a closed loop, continuously recycling 100% of the gas flow for reuse. Gas filtration and chemical getters are employed in the gas recycling path to minimize potential contamination of the gas stream from particles, hydrocarbons and water vapor.

To achieve the required EUV source power and repetition rate, a 1700 W laser driver has been developed by the TRW Inc. and integrated with the continuous jet target. The laser is a diode-pumped, solid state Nd^{3+}:YAG laser comprised of three identical laser modules, each of which produces 570 W of time-averaged 1.06 μm power at repetition rates of 1667-2000 Hz. The beams from the three modules are multiplexed to deliver 285-342 mJ/pulse at a combined repetition rate of 5000-6000 Hz, or can be synchronized to deliver 900 mJ/pulse at a repetition rate of 1667-2000 Hz. Pulse duration for each individual chain is ~6 ns FWHM and the beam quality, as determined by the focal spot size in the far field, is 1.1 – 1.2 times the diffraction limit. Laser beam pointing is actively controlled at 6000 Hz, achieving a total combined beam drift/jitter of approximately 0.25 times the diffraction-limited spot size. Output power stability is also excellent, exhibiting root-mean-square deviations ranging from 0.6-0.8%, depending on output power.

Table 2. Illumination System requirements for Engineering Test Stand	
Wavelength	13.4 nm
Total power incident on condenser	4.4 W over 1.8 sr and 2.5% spectral bandwidth
Power delivered to reticle	≥0.76 W
Repetition rate	≥3000 Hz
Illumination format	96 mm arc, ≤6 mm wide
Partial coherence	0.7
Illumination uniformity	±2%
Illumination stability	1% 1-sigma
Source motion	< ±25 μm
Condenser lifetime	≤10% reflectance loss after 10^{10} pulses

The 1700 W laser driver has been integrated with the continuous jet source and optimization of the EUV yield, and the nozzle thermal performance is in progress. Under 1260 W of incident laser irradiation, the laser-to-EUV conversion efficiency at 13.4 nm is measured to be 0.54 mJ_{EUV}/J_{laser}-eV-sr, yielding an output power of 9.8 Watts integrated over a 2.5% spectral bandwidth and 2π steradians. As shown in Fig. 3, this represents an increase in source power by a factor of more than 7.5 during the past year. Efforts are in progress to satisfy the source power requirement for the ETS by improving the laser beam delivery efficiency to increase laser power delivered to the jet target to 1500 W and also by reducing the attenuation of plasma source emission caused by residual Xe in the source chamber.

The jet assembly has been designed to keep the nozzle throat and mounting assembly cool during operation at full laser power. In addition, materials used for plasma-facing nozzle and vacuum hardware are chosen to minimize the rates of erosion and subsequent deposition of eroded material on nearby multilayer-coated optics. Experiments to establish the reflectance lifetime of the plasma-facing first condenser element as functions of laser pulse energy, average power, and nozzle-laser separation are in progress.

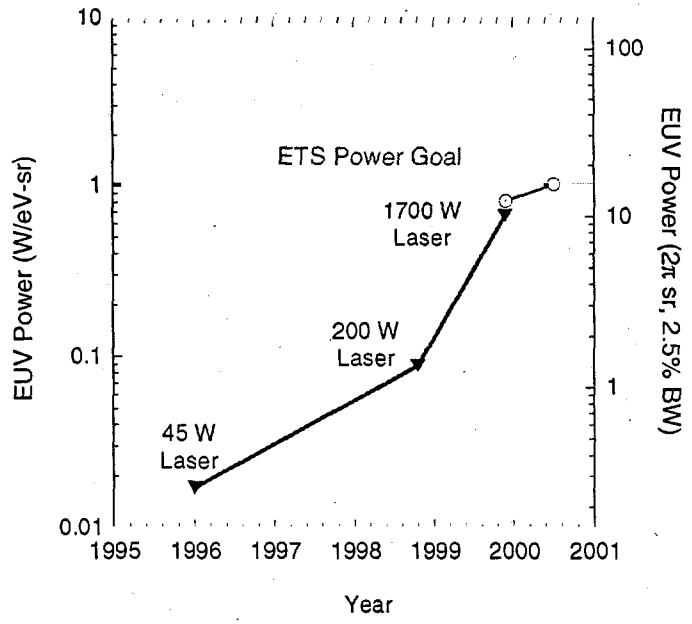

Figure 3. Recent progress in EUV power generation (solid triangles). In 1999 the EUV power was increased by more than a factor of 7.5 through the integration of the TRW 1700 W laser with the AES continuous Xe jet source. The eventual EUV power requirement (open circles) for the ETS is 15 W integrated over 2π sr and 2.5% spectral bandwidth.

3.2 Condenser optical design

The ETS condenser is a 19 element design that collects EUV radiation in 6 channels, intercepting a total solid angle of 1.68 sterradians (see Fig. 2). The condenser provides Kohler illumination along the arc field and critical illumination across the arc field in the scanning direction. This design achieves a high degree of uniformity along the arc in the cross-scan direction. Illumination from the 6 channels are combined within the pupil of the projection system, resulting in an effective fill factor of 0.7.

The C1 collector is comprised of 6 mirrors, each of which is a compound elliptical concentrator that focuses the collected radiation into a 55° arc focus. The mirrors are orientated in such a way that the pupil fill profile is synthesized at an intermediate pupil plane located at condenser element C3. In each channel a grazing-incidence flat mirror, C2, is aligned with a slightly-powered near-normal mirror, C3, to rotate the 6 arcs and superimpose them at a common location at the reticle plane. The final grazing-incidence mirror, C4, is an aspheric element that serves two functions. It reshapes the combined arc focus of EUV radiation from a 55° arc to a 30° arc, matching the projection system field of view in the reticle plane. The second function of C4 is to image the pupil fill profile at C3 into the aperture of the projection system at an effective fill factor of 0.7.

3.3 Illuminator mechanical design

The condenser mechanical design (See Fig.4) must maintain the positions of the 19 condenser mirrors to translational tolerances on the order of 60 microns and angular tolerances of 40 microradians. Additionally, the C1 assembly and the C3 assembly must be easily replaced since they are consumable in the ETS operation. The stability requirements were met by isolating the entire condenser from the walls of the vacuum chamber, to minimize motion from pump-down and to mitigate acoustic and pump vibrations. To minimize thermal distortion of the optics, the C1 assembly is water-cooled and the individual substrates are made of silicon for high thermal conductivity. The C3 assembly has passive cooling.

The C1 and C3 assemblies are kinematically mounted and readily replaceable. Pre-alignment stations were designed, fabricated, and tested in parallel with the illuminator fabrication. These alignment stations are used to pre-align the C1 and C3 assemblies relative to their kinematic mounts while the illuminator remains operational. As a result, replacing a C1 or C3 assembly is analogous to replacing a single optic. The pre-alignment of the assemblies has been demonstrated and no re-alignment of the illuminator is required when these optics are replaced.

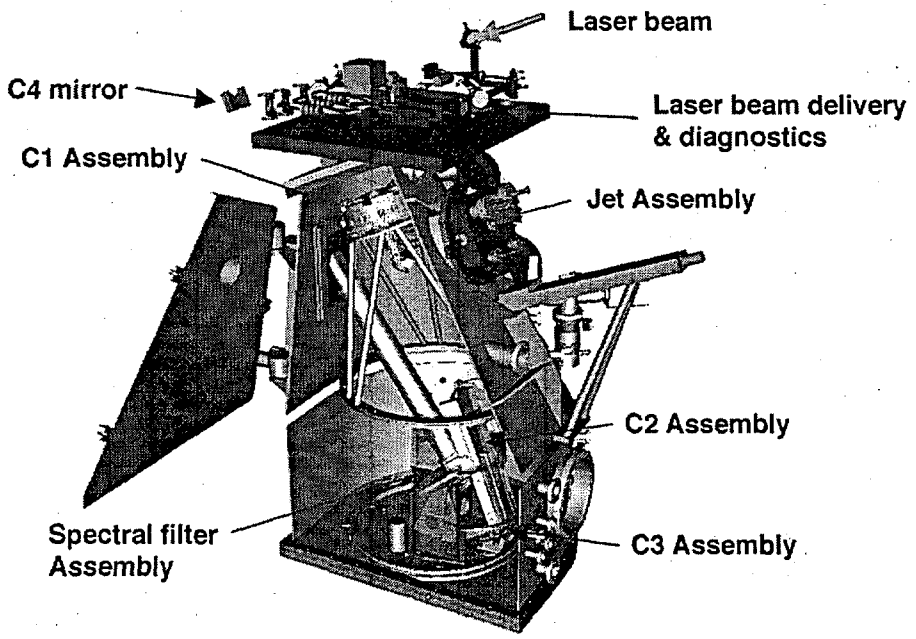

Figure 4. Engineering model of the high-power EUV illumination system developed for the Engineering Test Stand.

Successful operation of the illuminator requires simultaneous operation of the laser produced plasma source, alignment of all 19 elements of the condenser as well as the spectral purity filter, and environmental protection for the optics.

3.4 Illuminator Characterization

The pupil chamber was fabricated to evaluate the illuminator before the main enclosure fabrication and assembly was complete. The pupil chamber provides a vacuum enclosure for the C4 mirror, a reticle stage with EUV diagnostics, and a gadolinium oxysulfide scintillator plate at pupil plane. The reticle stage is an off-the-shelf in-vacuum stage used for translating diagnostics and a multilayer-coated mirror through the EUV light at the reticle plane. The diagnostics are 4 individual EUV dose sensors. These sensors have a very large dynamic range (10^4) and are able to directly measure the EUV output without attenuation. The multilayer-coated mirror is used to reflect the EUV light to the pupil plane at the bottom of the pupil chamber where it is recorded via EUV-induced scintillation.

The environmental requirements for operating the illumination system are to minimize high mass hydrocarbons and to implement a protective gas blend before each EUV operation. High mass hydrocarbons are defined as anything above atomic mass 44. For the illuminator and pupil chamber the partial pressure of the hydrocarbons above mass 44 were on the order of 1e-11 torr. This level was deemed acceptable for EUV operations. The gas blend is a formula developed to protect all EUV-exposed multilayer coatings from oxidation by residual water vapor. The formula specifies a 2:1 ratio of ethanol to water based on partial pressure measurements. The gas blend was implemented and the plasma was initiated.

Following visible-light alignment of the condenser using the diamond-turned aluminum C1 surrogates, the multilayer-coated C1 assembly was installed in the illumination chamber and the ethanol gas blend was implemented. All of the mechanical degrees of freedom in the source-condenser optical train, except the position of the plasma source relative to the C1, focus were "frozen" via previous optical and mechanical alignment using a coordinate measuring machine. The alignment of the six condenser channels was then monitored at the pupil plane as the plasma source centroid was translated slightly by moving the gas jet and laser focal position. The source was run at a repetition rate of 10 Hz to allow facile viewing of the resulting

illumination patterns for alignment. Reasonable EUV alignment was achieved ~20 min after the source was ignited. A representative image of the illumination at the pupil plane, recorded via EUV-induced scintillation from a gadolinium oxysulfide scintillator plate, is shown in Fig. 5. A simulated pupil fill, calculated in Code V for a point source, is provided for comparison. In both the simulated and actual images, the circle represents sigma = 0.7 (70% of the pupil diameter). As can be seen in the figure, the qualitative aspects of the pupil fill are well-matched to the prediction. Differences due to the finite source size and less uniform angular distribution of the continuous jet source are being quantified. The thin horizontal bands in the experimental image are caused by shadows from the blades of the fast EUV shutter.

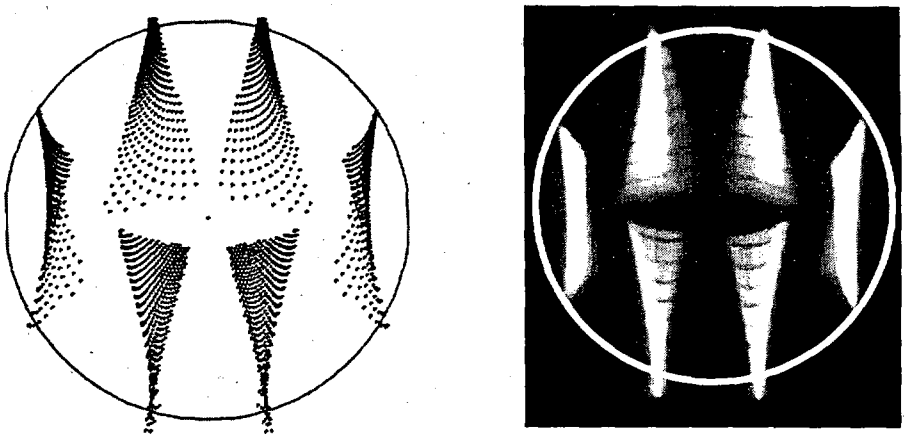

Figure 5. Comparison of pupil fill as predicted using Code V and a photo taken of EUV scintillation from a gadolinium oxysulfide scintillator plate.

4. PROJECTION SUBSYSTEM

The ETS projection system is designed to demonstrate the printing of full-field images at 100 nm resolution in step-and-scan mode. Having a numerical aperture of 0.1, the projection system also meets the requirements for printing of 70 nm dense lines and spaces at a k_1 value of 0.52.

4.1 Projection optics design

The projection optics is a 4-mirror ring-field design[5,6], with a 4× reduction, that is shown schematically in Fig. 6. The numerical aperture is 0.1, which readily supports printing 100 nm design rules at an EUV wavelength of 13.4 nm. The optical design consists of four mirrors labeled M1, M2, M3, and M4 in Fig. 6. Three of the mirrors are aspheric and M3 is a sphere. The aperture stop is located at M3. The overall length from the mask plane to the wafer plane is 1075 mm. The design is rotationally symmetric, and the well-corrected field is an annulus extending over a radial range from 208 mm to 214 mm in the mask plane. The used field is a 30° arc of this annulus, which corresponds to a chord length of 104 mm at the mask. Images will be printed by synchronously scanning the wafer at a quarter of the velocity of the mask, so that the moving image will appear stationary on the wafer. Of the full rotationally symmetric aspheric parent, only a region around the actual used clear aperture was manufactured, to minimize the weight of the substrates and improve their mounting stability.

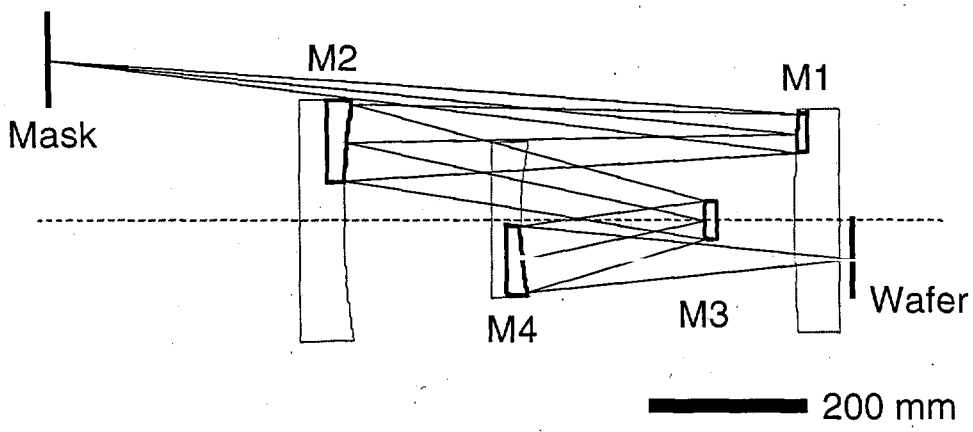

Figure. 6. Schematic diagram of the EUV lithographic camera, showing the used segments of the mirrors (bold outlines) as well as the rotationally symmetric parents from which they were derived (thin outlines). Mirror M3 is a sphere and the others are aspheres. The pupil is located at M3. The well-corrected field is an arc of an annulus centered on the optic axis. Rays are shown for one field point.

The optical design was optimized with the aim of simultaneously satisfying several design constraints. These design goals included wavefront quality, reduction ratio, telecentricity, field curvature, image distortion, aspheric departure, and control of incidence angles on the mirrors. This last constraint was to allow uniform, rather than graded, multilayer coatings on the mirrors, and was achieved by using one multilayer *d*-spacing on the aspheres and a slightly larger *d*-spacing on M3 where the average angles of incidence are higher. The aberration correction is dominated by the behavior of astigmatism. By controlling the high-order aspheric terms on the mirrors, both 5^{th} and 7^{th} order astigmatism was brought to zero at the center of the ring field. The design wavefront error at this point is 0.004 waves and 0.020 waves at top and bottom of the ring-field, for a wavelength of 13.4 nm. The distortion was controlled so that the magnification as a function of field radius has a stationary point at the center of the ring field. This "balanced" distortion minimizes the blurring of the scanned image caused by image distorion. It is found that although the static distortion field has a maximum magnitude of 16 nm, scanning through this field leads to a scan blur that reduces the Strehl ratio by only 0.007, with a residual dynamic distortion of less than 2 nm. The design is telecentric at the wafer, but since the mask is reflective, the imaging at the mask is necessarily oblique. This characteristic imparts stringent flatness requirements on the mask, but it does allow a residual magnification control of ±20 ppm to be achieved simply by varying the conjugate plane locations.

4.2 Projection Optics Box Mechanical Design

The projection optics box (POB) is made up of an assembly of four optics each supported in optic cells, 10 remotely actuated adjustments, a main structure, a host of sensors and a control system. The mechanical design of the POB is driven by the need to achieve and maintain precise alignment among the optics and to isolate the optics from forces and movements that would distort their figure. The design philosophy attempts to keep the POB imaging system completely passive other than the actuated adjustments, the objective being to avoid active thermal or mirror positioning control. This is achieved by designing for high resonant frequencies, using low CTE (coefficient of thermal expansion) material, and taking advantage of the long thermal time constants inherent with large thermal masses and radiative heat transfer between the POB and ETS chamber.

4.2.1 Optical Mount Design

All optical mounts use an exact constraint design approach. In each mount design, three bipod flexures are used to fully constrain the six rigid-body degrees of freedom of a substrate with respect to a rigid optic cell. Figure 7 shows a typical optic cell design with the various components noted.

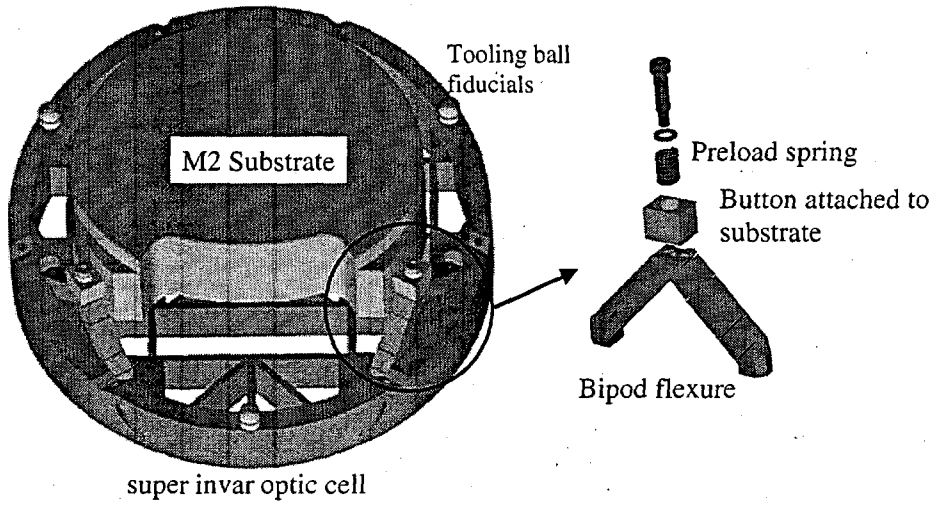

Figure 7. Typical optical mount cell.

Each leg of the bipod flexure is designed to have high stiffness along its axis or constraint direction and much lower stiffness in all other directions. The connection of the bipod to a substrate is designed to allow the substrate to be removed from the mount cell. In the figure, the bipod is shown along with a button that is bonded to the substrate. The button and bipod connect through a coupling design that insures a highly repeatable, fully constrained joint. Another common component of all the mount designs is a rigid optic cell that serves to fix the mount bipods with respect to one another and to act as an interface to other structures. The optic cells are designed to provide a rigid, stable platform for the optics.

4.2.2. Projection Optics Box Structure Design

The POB structure appears in Figure 8. The POB structure is a Super Invar weldment consisting of three horizontal plates and bent side walls. Openings in the sides allow access to the inside first for welding the structure then for assembling the many components within the POB. The major design goals are: 1) to provide high dimensional stability, 2) to provide access to assembled optical cells within the POB, 3) to facilitate coarse alignment of the optics, and 4) to be relatively compact, an aspect that ripples through the design of the ETS and system metrology facilities and contributes to good structural dynamics and low temperature gradients. The POB structure is 514.3 mm (20.25 in.) wide by 549.4 mm (21.63 in.) deep by 618.5 mm (24.35 in.) tall and weighs approximately 191 kg (420 pounds) fully assembled.

Finite element analysis (FEA) has been used throughout the design of the POB structure, optic mounts and actuation systems. This model was used to compare with the experimental modal analysis of the assembled POB system for free-free boundary conditions. Table 3 shows the correlation to be very good. In addition, the animated mode shapes of the FEA match those of the experiment. As expected, all the modes of the unconstrained system are very lightly damped, in the range from 0.1% to 0.6% of critical damping.

Table 3. Comparison of experimental versus FEA modal frequencies.

Mode	Experimental Measurement	FEA Prediction	% difference
1	142 Hz	145 Hz	2.10%
2	169 Hz	171 Hz	1.20%
3	178 Hz	184 Hz	3.40%
4	190 Hz	194 Hz	2.10%
5	241 Hz	240 Hz	0.04%
6	257 Hz	254 Hz	1.10%
7	296 Hz	297 Hz	0.04%

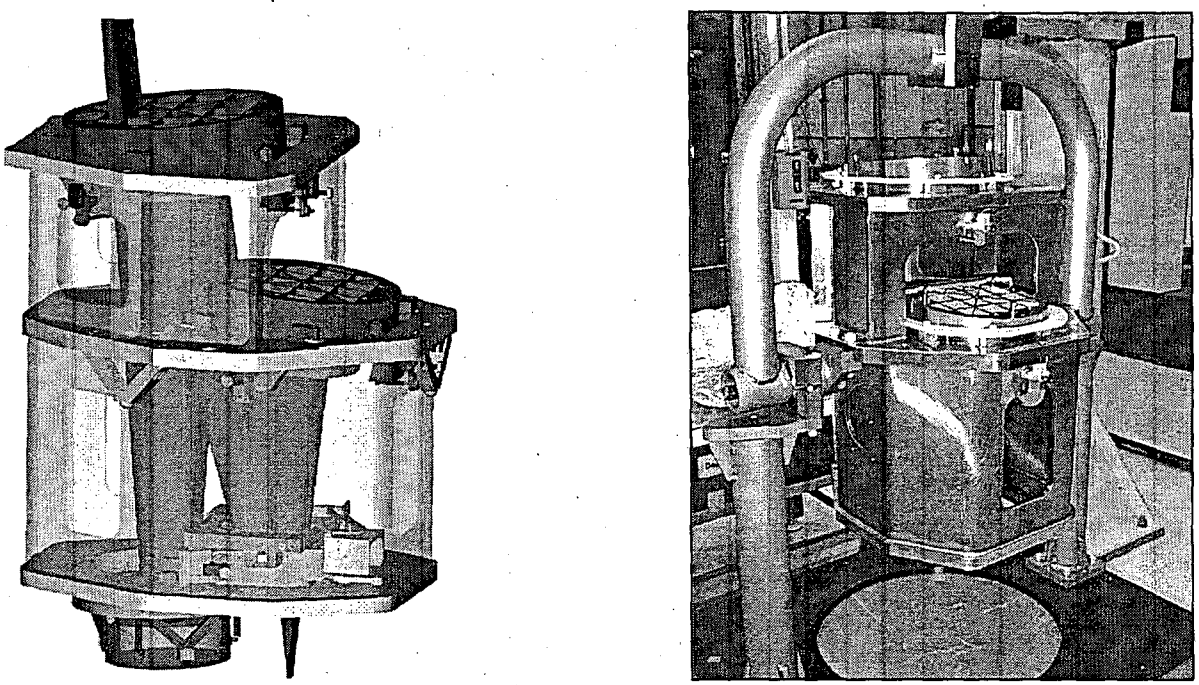

Figure 8. POB assembly shown with optic cells and actuation systems.

4.3 Projection optics box alignment

The POB was assembled in a two-stage process. The first step was a mechanical assembly of the mirrors using a CMM, and the second step was optical alignment using a visible-light point-diffraction phase-shifting interferometer (also known as a Sommargren interferometer[7]). The optical alignment was based on a detailed and rigorous procedure[8], and finds the rigid-body adjustments of the mirrors required to correct for wavefront aberrations and image distortion measured at many points across the ring field. This method determined which of the rigid-body degrees of freedom should be used in the alignment process. These are a small subset of the total 24 possible degrees of freedom of the four mirrors and are those which address the most linearly independent set of aberration modes. Eight degrees of freedom were identified (tip, tilts and piston on mirrors M2 and M4; x y translation on M3) that could be used to correct all misalignment modes, providing that the magnitude of the aberration after mechanical assembly did not exceed about 50 nm, rms (this is referred to as the capture tolerance of the alignment). This choice of compensators set the specification on the accuracy of the initial alignment and on the design of the mounts. To achieve this accuracy required knowing the location of the aspheric surface (in all six degrees of freedom) relative to measurable fiducials on each of the substrates. This was achieved with the use of precisely characterized masks that were common to both interferometric surface figure measurements and CMM measurements of the mirror substrates, as well as by making contact measurements of the mirrors just outside their clear aperture. The estimated errors in locating the aspheric surfaces within the POB were of the order 5–10 μm in translation and 100 μrad in orientation. The mirrors were assembled in the POB according to a recompensation of the original design, based on the measured figure errors of the mirrors. This recompensation identified positions and orientations of the optics that would give optimum performance for scanned images.

4.3. 1. Mechanical Assembly

The four projection optics must be mechanically assembled within the POB structure to specified capture tolerances. The capture tolerances describe the deviation from the optical design location allowed for each of the optical surfaces. The capture tolerances of a typical aspheric optic are given in Table 4 along with an estimate of the accuracy with which they are likely to be placed. Confirmation that the mechanical alignment was well within capture tolerances came from the optical alignment station where the wavefront error was measured to be approximately 5 nm rms as delivered.

Table 4. Capture tolerances for mechanical assembly.

Degree of Freedom	Capture Tolerance	Estimated Accuracy
X	±110 μm	±80 μm
Y	±110 μm	±80 μm
Z	±270 μm	±20 μm
θ_x	±220 μrad	±60 μrad
θ_y	±220 μrad	±60 μrad

The primary metrology tool used during mechanical assembly is a coordinate measuring machine (CMM). However, the CMM is not accurate enough to determine the x-y location of the vertex of a very mild asphere to within the capture tolerances. The vertex must be located with the interferometer and related back to physical datum surfaces on the optic. This information combined with CMM measurements around the clear aperture of the optic is sufficient to establish the optical coordinate system. Since the optical surfaces are not readily accessible in the assembled POB, three tooling balls on each optic cell are located in the optical coordinate system. Figure 9 shows this mapping process for the M4 optic. The tooling balls are very accessible in the assembled POB as Figure 9 shows. A geometric model that incorporates the optical design, mapping information and the measured locations of the tooling balls computes the position errors of the optics and the required mechanical adjustments to correct the errors. With just a few iterations, the mechanical alignment converges to approximately 5 microns in z and 10 microns in x and y, not including the positioning error in the CMM and the uncertainty of the vertex location.

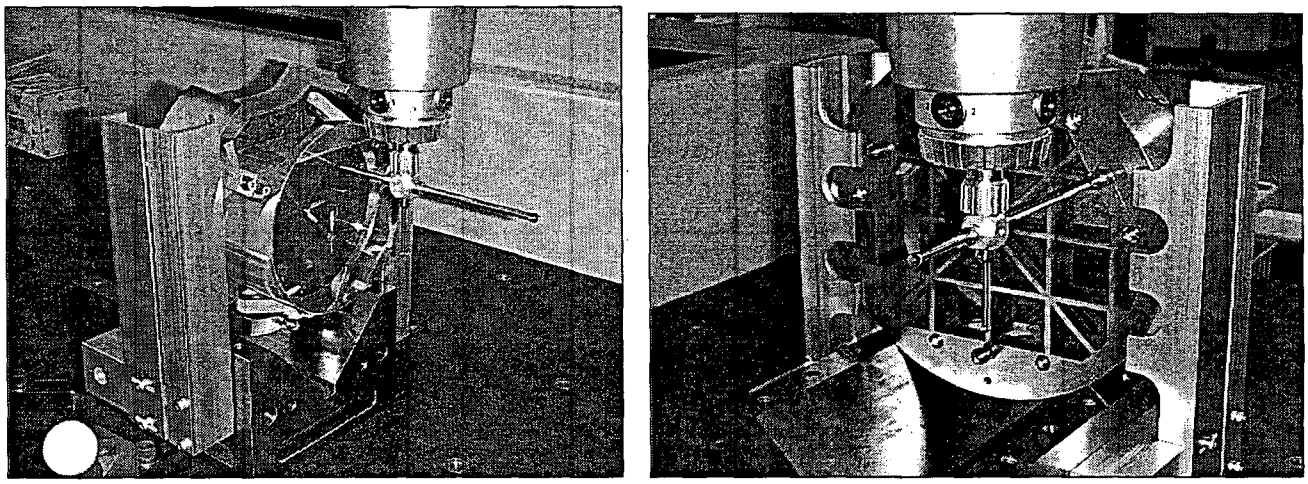

Figure 9. The CMM measurements of the M4 optical surface (left) and tooling ball locations (right) required for the mapping process.

4.3.2. Optical alignment

The alignment interferometer is a phase-shifting point-diffraction interferometer that makes single-pass measurements of the projection optics' wavefront at various locations in the ring field and can also determine image distortion at those locations. The test beam of the interferometer is diffracted from a pinhole located at the wafer plane and imaged by the projection optics to the mask plane. Here it reflects, and combines with the reference beam, which is diffracted from a pinhole in the mask plane. The two beams interfere at a CCD camera, which is imaging the pupil of the projection optics. Various points in the field are sampled by diffracting the test and reference beams through appropriate pairs of pinholes located among an array of pinholes that span the entire ring field. The pinholes at the mask and wafer planes are arranged in an array of 45 points. The use of arrays of pinholes enables image distortion measurements to be made. The two tilt terms of the interferogram are directly proportional to the *x* and *y* vector displacement between the reference-beam pinhole and the image of the test-beam pinhole. The relative coordinates of all pinholes were measured to an accuracy of 12 nm using a Leica IPRO mask inspection tool. This allows the variation of tilt across the field to be calibrated for actual pinhole location in order to determine the image shift induced by the projection optics. We estimate the accuracy of the interferometer to be better than 0.20 nm rms for wavefront and 150 nm rms for image-plane distortion. The distortion accuracy is currently about a factor of four times

larger than required, and improvements are being made to reduce errors caused mainly by drift of the pinhole arrays and illumination system.

Upon mechanical assembly, the first measured wavefront through the projection optics had a wavefront aberration of only 5.0 nm rms. An alignment correction was computed, based on wavefront and distortion measurements made at 15 field points. In the correction the mask and wafer degrees of freedom were allowed to vary, in addition to the eight projection optics adjustments, in order to locate the best conjugate planes. Prior to making the correction, all degrees of freedom were calibrated by making an adjustment of each degree of freedom in turn and comparing the observed aberration change to the modeled aberration sensitivity. As well as calibrating the magnitudes and signs of the adjustments, cross coupling of adjustments was also found and accounted for. The alignment correction required adjustment of all degrees of freedom in order to correct the field-dependent wavefront aberration and image distortion. The correction was performed and the aberrations were corrected as expected. The final wavefront was well corrected across the field, with a mean wavefront aberration of 1.3 nm, and a minimum aberration of 0.95 nm near the center of the field. The alignment also removed 40 ppm of magnification error and reduced the mean image-plane distortion from 350 nm to 150 nm. A plot of the wavefront aberration, measured at 45 points across the field, is shown in Fig. 10.

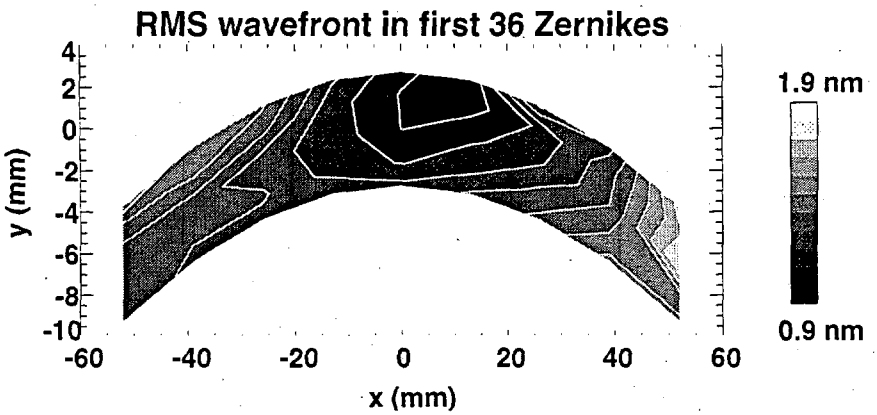

Figure 10. Measured rms wavefront error as a function of field location at the mask plane, as measured in the visible-light alignment interferometer.

5. STAGE SUBSYSTEM

The wafer and reticle stage subsystem consists of the reticle and wafer stages, metrology for each stage, and control electronics. The stage support structures (bridge), vibration isolation system, and isolated frame of the ETS main chamber are critical to stage performance and are included in all stage subsystem analysis. The combination of the wafer stage, reticle stage, and bridge provide a stable, stiff platform that allows the wafer and reticle to be positioned to the tight tolerance required for EUVL. The wafer stage must track the reticle stage during scanning of the reticle stage through the EUV field. Tight tolerance is placed on the tracking performance to assure minimum influence to image position repeatability and distortion. A feedback control system controls the synchronization of the reticle and wafer stages for scanning the die site during EUV exposure. Throughput, structural stability, optical capability, and wafer exposure characteristics determine stage subsystem specifications for acceleration, scan speed, settle time, and dynamic stability. Magnetically levitated (maglev) stages have been chosen as the lowest-risk approach to addressing the performance and vacuum requirements. Testing of the prototype wafer and reticle stages indicates that the stage system will meet ETS performance specifications.

A model of the ETS structures, stages, and controls was created to predict performance of the stage subsystem and to serve as a tool in formulating and comparing control algorithms. It incorporates information from the ETS system structural dynamics model and the optical model to yield system performance predictions. Early model results, along with validation experiments, contributed to ETS design decisions in the areas of stage control, vibration isolation, and overall machine configuration.

5.1 Maglev Stages

The vacuum environment required for EUVL requires a stage design that minimizes contamination of the object reticle, target wafer, and machine optics. 1D-long-travel maglev stages based on demonstrated concepts[9,10] have been chosen for this application. Maglev offers the advantages of low power and low particle generation, and has been demonstrated in the fine position stage used in the 10X Microstepper.[11]

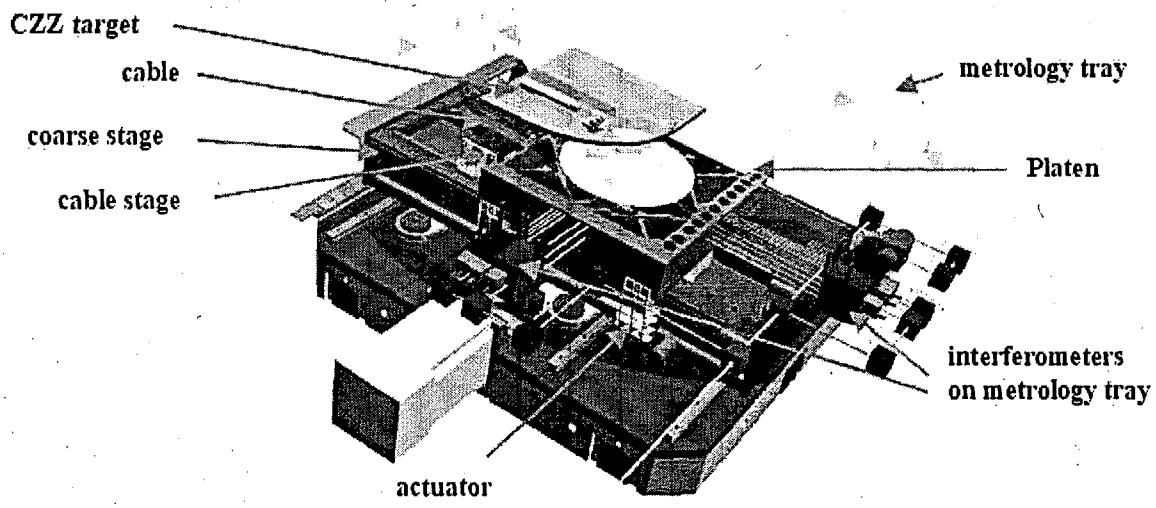

Figure 11. Wafer stage model including interferometry.

The wafer stage (Figure 11) consists of the stage base, off-axis coarse stage (the beam of the maglev stage), levitated platen, cable stage, and wafer chuck. The reticle stage (Figure 12) is identical to the wafer stage without the off-axis coarse stage and is mounted in an inverted position. Each stage includes an electrostatic chuck for holding a wafer or reticle. The monolithic platen is magnetically suspended from the beam and carries image diagnostic and alignment sensors.

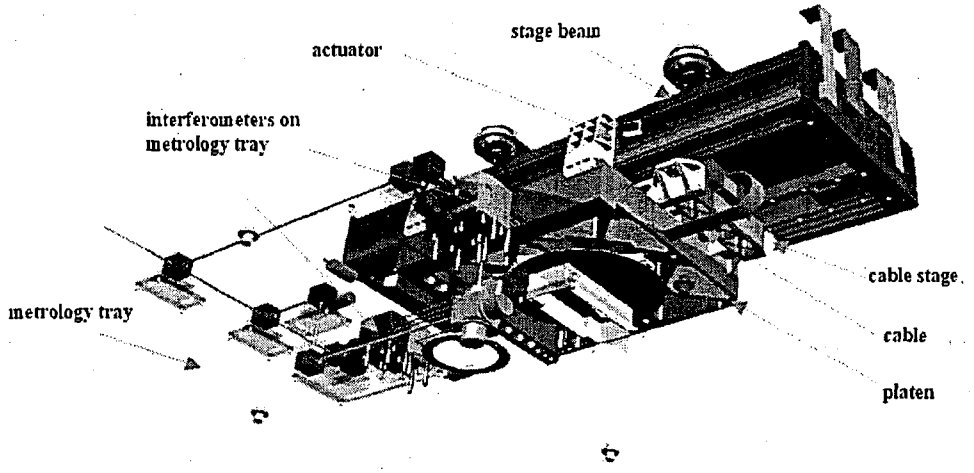

Figure 12. Reticle stage model including interferometry.

Included in the stage design is a cable stage that moves on linear guides and is designed to reduce the disturbance forces imparted on the scanning stage by rolling cables.

5.2 Stage control

The stage controller is implemented in software that runs on several real-time embedded computers. The controller compares the measured positions of the two stages with their desired positions and attempts to drive these errors to zero by a combination of feedback and feedforward strategies. The hardware and software used to control the ETS stages is a

combination of commercially available electronics, custom electronics, and software routines and drivers specifically configured to perform tasks necessary to interface to stage system sensors and actuators, and execute the necessary control algorithms. Position accuracy of the stages during EUV exposure is dependent on many factors. These contributing factors include: the stiffness of the overall structures and stages, the accuracy and precision of all feedback sensors, associated electronics, and the control strategy used to manipulate the sensor based information.

5.3 Performance results

Stage performance has been evaluated using a prototype wafer stage using a configuration that approximates the structural properties of the ETS known as the Stage Development System (SDS). The ETS requires that the jitter of each stage as referenced to the POB always be less than 10nm rms and the mean tracking error must always be less than ±3nm. Performance results (Figure 13) from the SDS show jitter less than 4.5nm rms and mean tracking error less than 1.5nm are achievable for the ETS.

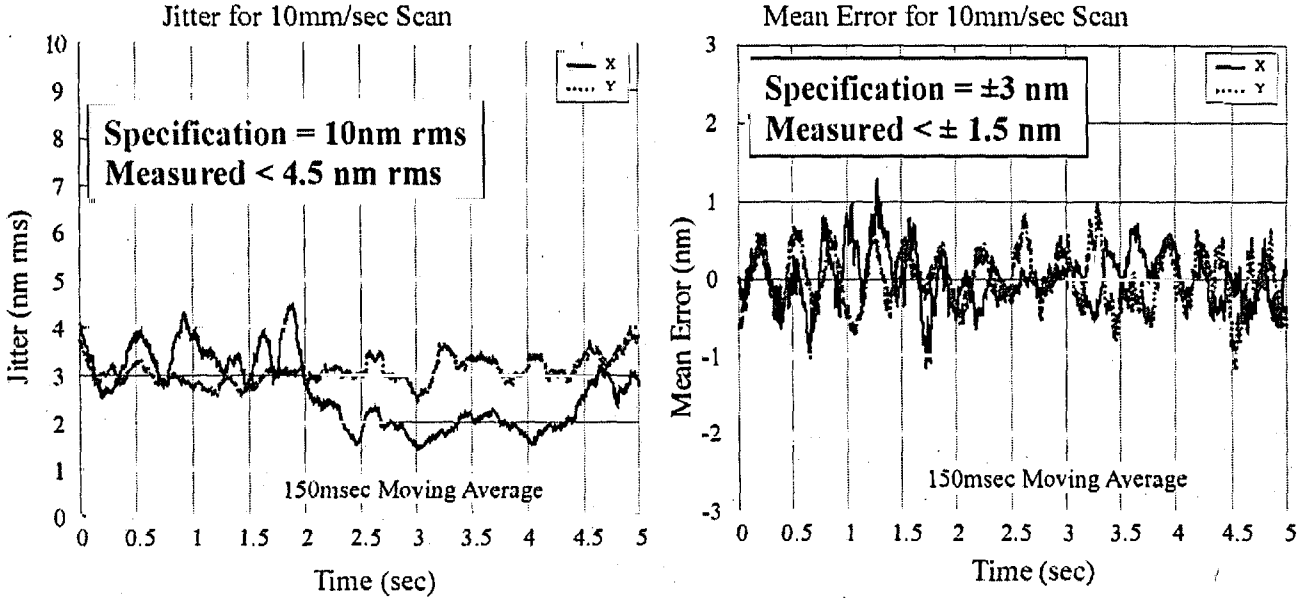

Figure 13. Wafer stage jitter and mean tracking error for 10mm/sec scan for prototype test stage.

6. ENVIRONMENTAL SUBSYSTEM

The ETS environmental system is engineered to minimize particulate and chemical contamination of sensitive lithographic components such as optics and the reticle. The ETS Main Chamber is divided into three environmental zones. (See Fig. 14) These zones are called the Reticle Zone, the Optics Zone and the Wafer Zone. Each zone is an individually controllable vacuum environment.

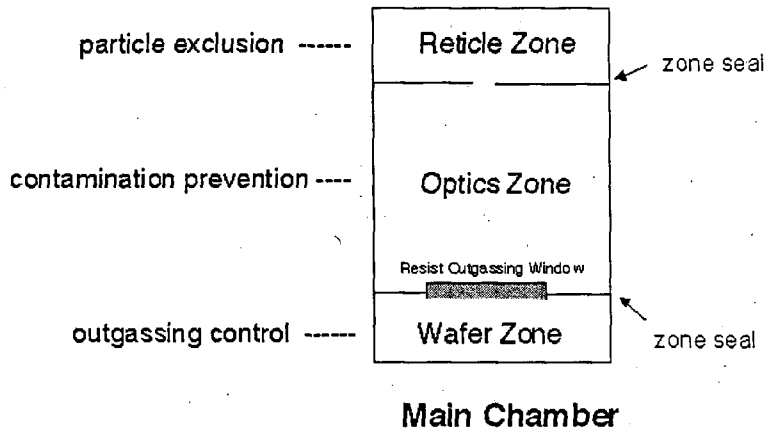

Figure 14. Schematic of ETS environmental system.

In the Reticle Zone, conditions are maintained to allow operation of thermophoretic[12] reticle protection via the Klebanoff-Rader "pellicle." The Klebanoff-Rader approach affords robust protection (> 10^6) of the reticle from particles during lithographic operation. Other virtues of the thermophoretic protection scheme are high EUV transmittance and intrinsic cleanliness. The Reticle Zone is isolated from the Optics Zone via a slot that allows entry and exit of EUV radiation. The slot acts as a differential pumping stage, allowing an elevated pressure in the Reticle Zone (needed for thermophoretic protection) while maintaining a reduced pressure in the Optics Zone (needed for high EUV transmission).

In the Optics Zone, the chief environmental concern is carbon and oxygen deposition on the optics caused by EUV "cracking" of residual hydrocarbon and water molecules in the gas-phase environment. The ETS is being constructed from materials and components that have been carefully selected and screened for low hydrocarbon outgassing. The Optics Zone will allow contamination prevention methods to be deployed, for example the use of ethanol in a "Gas Blend" to prevent optic oxidation.

The Wafer Zone is a completely separate vacuum environment with no vacuum communication to the other two zones. The purpose of the Wafer Zone is to prevent photoresist outgassing from contaminating optics in the Optics Zone. A Resist Outgassing Window resides above the wafer and allows the entry of EUV radiation while intercepting any EUV-induced photoresist outgassing.

7. OPTICS FABRICATION

7.1 Specifications

The ETS projection optics substrates have stringent specifications on both figure and finish, which present substantial challenges for optics manufacturers. We divide these specifications into three categories that correspond to the key functional requirements of the imaging system: figure, Mid-Spatial Frequency Roughness (MSFR), and High-Spatial Frequency Roughness (HSFR).[13] Each category is defined as the integral of the two-dimensional power spectral density of surface errors over specific ranges of spatial frequency. The definitions of each category and their respective functional requirements are given in Table 5. Because the specifications are tied to a specific optical design and performance requirement, it is important to note that these specifications relate to absolute accuracy, as opposed to the precision with which the optical surface matches a reference artifact. The ETS has been designed to achieve diffraction-limited imaging with good contrast and high reflectivity. The specifications for the ETS substrates that support these requirements are listed in Table 5 under the heading 'Set 2 Specifications'.

Table 5. Specifications and measurements for ETS optical substrates.

Error Term (Relates to Absolute Accuracy)	Functional Metric	Spatial Frequency Definition	Set 1 Spec Intermediate (nm rms)	Set 1 (ave) Measured (nm rms)	Set 2 Spec ETS (nm rms)
Figure	Resolution Distortion	$(CA)^{-1}$ – 1 mm^{-1}	0.50	0.50	0.25
Mid-spatial frequency roughness (MSFR)	Flare Contrast	1 mm^{-1} – 1 μm^{-1}	0.50	0.27	0.20
High-spatial frequency roughness (HSFR)	Throughput Loss	1 μm^{-1} – 50 μm^{-1}	0.40	0.16	0.10

7.2 Metrology

The measurement of errors in the three key specification categories corresponds to the ranges of spatial frequencies typically sampled by three key types of instruments. For measuring absolute figure accuracy over the full clear aperture, we have designed and constructed a novel interferometer, the Phase-Shifting Diffraction Interferometer[14] (PSDI). It employs nearly perfect spherical waves generated by propagating both the reference and test waves through small diffracting apertures. Our detailed analysis of both systematic and non-repeatable error sources supports the certification of surfaces with 0.25 nm rms absolute accuracy when measuring aspheric ETS substrates. Measurements of MSFR and HSFR are performed using a commercial phase-measuring interferometric microscope and a commercial atomic force microscope, respectively. The accuracy of these roughness measuring instruments has been validated by comparing the power spectral density (PSD) of the surface errors calculated from the measured profiles with PSDs determined from angle-resolved light scattering measurements performed at the Advanced Light Source.[15]

7.3 Progress in Fabricating Optics for the ETS

Simultaneously meeting the stringent ETS figure and finish specifications poses extreme challenges for optics manufacturers. Three of the four substrates are aspheric (order of 5 μm departure), which typically compounds the difficulty in attaining low roughness while attaining figure. At the beginning of the project, the Set 2 specifications were well beyond the state of the art in optical fabrication. During the past three years, however, the vendor(s) that we have been working with have carried out substantial developments and are currently fabricating surfaces that meet those specifications. In order to support the ETS development schedule, we are acquiring two sets of substrates, one to final ETS specifications referred to as the Set 2

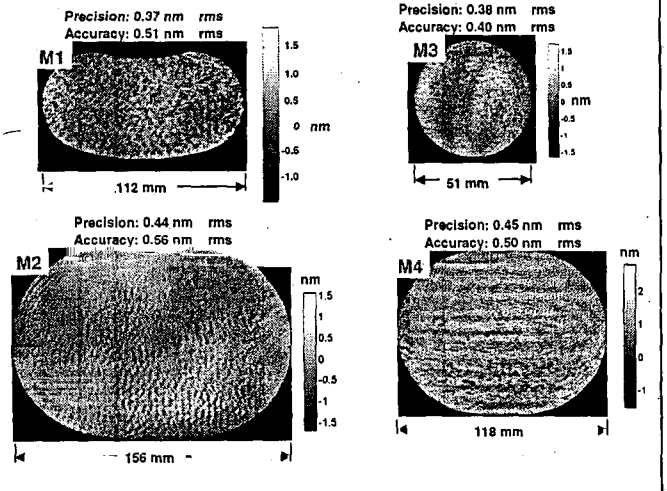

Figure 15. Measured surface errors for the ETS Set 1 optics. Precision refers to the direct instrument reading and accuracy incorporates known systematic errors.

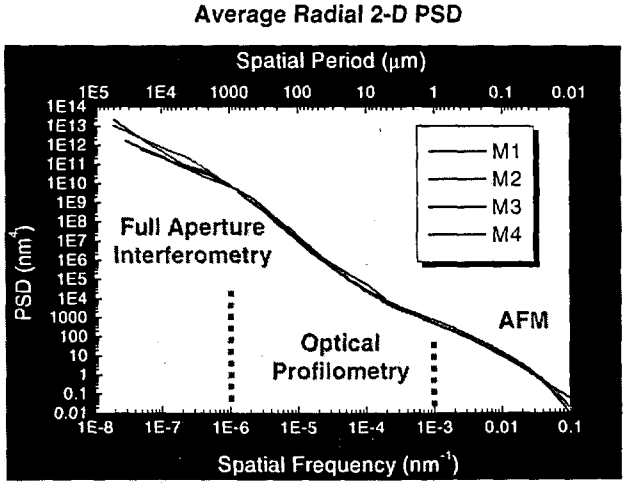

Figure 16. PSDs from metrology data for the Set 1 ETS optics. (coutesy of Eric Gullikson of LBNL)

optics, and a preliminary set specified to looser tolerances, the Set 1 optics. Specifications for each set are listed in Table 5. The specifications for the Set 1 optics were chosen to coincide with the anticipated progress of the development program at the vendor facility, as well as the concurrent development of the PSDI.

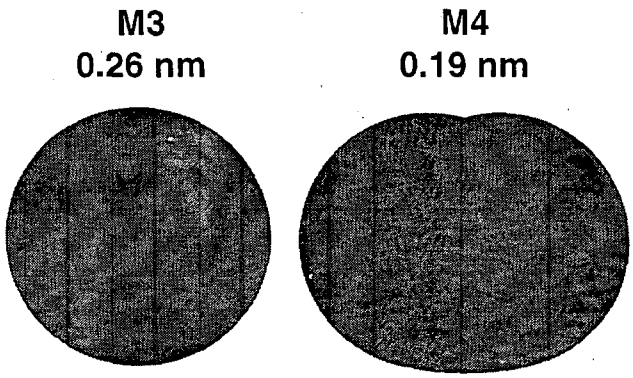

Figure 17. In-process figure measurements of the Set 2 ETS substrates M3 and M4. M3 is spherical and M4 is aspherical. (courtesy of SVG-Tinsley)

We have taken delivery of all of the Set 1 optics, which have been subsequently coated with multilayers and assembled in a POB, as described elsewhere in this manuscript. The figure error height maps of the Set 1 optics are shown in Figure 15, where total rms power for both precision and accuracy are listed. The precision value reflects the vendor's ability to converge to the measurement instrument, which was the prime focus of the Set 1 substrates. The accuracy term incorporates an estimate of systematic errors. Substrates M1 and M3 were measured using the vendor's interferometer, while M2 and M4 were measured using the PSDI, which was being concurrently developed. MSFR and HSFR were measured and were considerably smoother than the Set 1 specifications. Given data from all measurement categories, we calculated the PSD for each of the substrates, which are plotted in Figure 16. Although the ordinate axis covers many orders of magnitude, there is remarkable agreement among the curves over the regions labeled 'Optical Profilometry' and 'AFM', which suggests a deterministic approach for attaining low roughness. Somewhat larger variations in the figure region of the PSDs may indicate the varying degrees of difficulty associated with the different substrate geometries. The average value of the residual errors for all substrates and specifications are listed in Table 5.

The Set 2 substrates for the ETS are nearing completion to the more stringent specifications. The PSDIs for measuring each of the four substrates have been upgraded to achieve lower systematic errors. In-process measurements of the spherical M3 substrate and the aspheric M4 substrate are shown in Figure 17. M3 shows a figure error of 0.26 nm rms while the M4 was measured to be 0.19 nm rms. These are the direct readings from the instrument and are currently being analyzed for systematic errors. Both of these substrates will undergo continued processing for further improvement. The remaining Set 2 substrates are also under fabrication with final delivery and coating scheduled for mid-2000.

8.0 MULTILAYER COATINGS

Multilayers are deposited in DC-magnetron sputtering systems as described previously.[16] To preserve the figure of the projection optics, thickness control to about 0.1% rms is necessary. All four projection optics of the first set were successfully coated with high-reflectance Mo/Si multilayers within a ±0.1% peak-to-valley (P-V) tolerance across the clear aperture (shaded areas in Fig. 18 (a)-(d)).[17] In fact, the thickness variation is less than 0.1% P-V (±0.05% P-V) on all four optics. This represents a thickness difference that is commensurate with the size of *only one atom* for the full 40-bilayer stack across the clear aperture of the optics, the largest of which is 160 mm wide. The dashed lines in Fig. 18 (a)-(d) show the best quadratic fit to the data. A quadratic, or spherical, figure error induces a tilt and a focal shift that are easily compensated during optical alignment. Non-spherical figure errors, however, induce wavefront errors that cannot be corrected. The difference between the best quadratic fit and the measured thickness distribution for all four optics cumulates to less than 0.07 nm rms of non-correctable aspheric errors. This is well within the current specification of the optics and, therefore, the error will produce negligible multilayer-induced wavefront errors. The peak reflectance was measured to be 65.3±0.3% at a centroid wavelength of 13.33±0.03 nm as measured at their nominal angles of incidence.

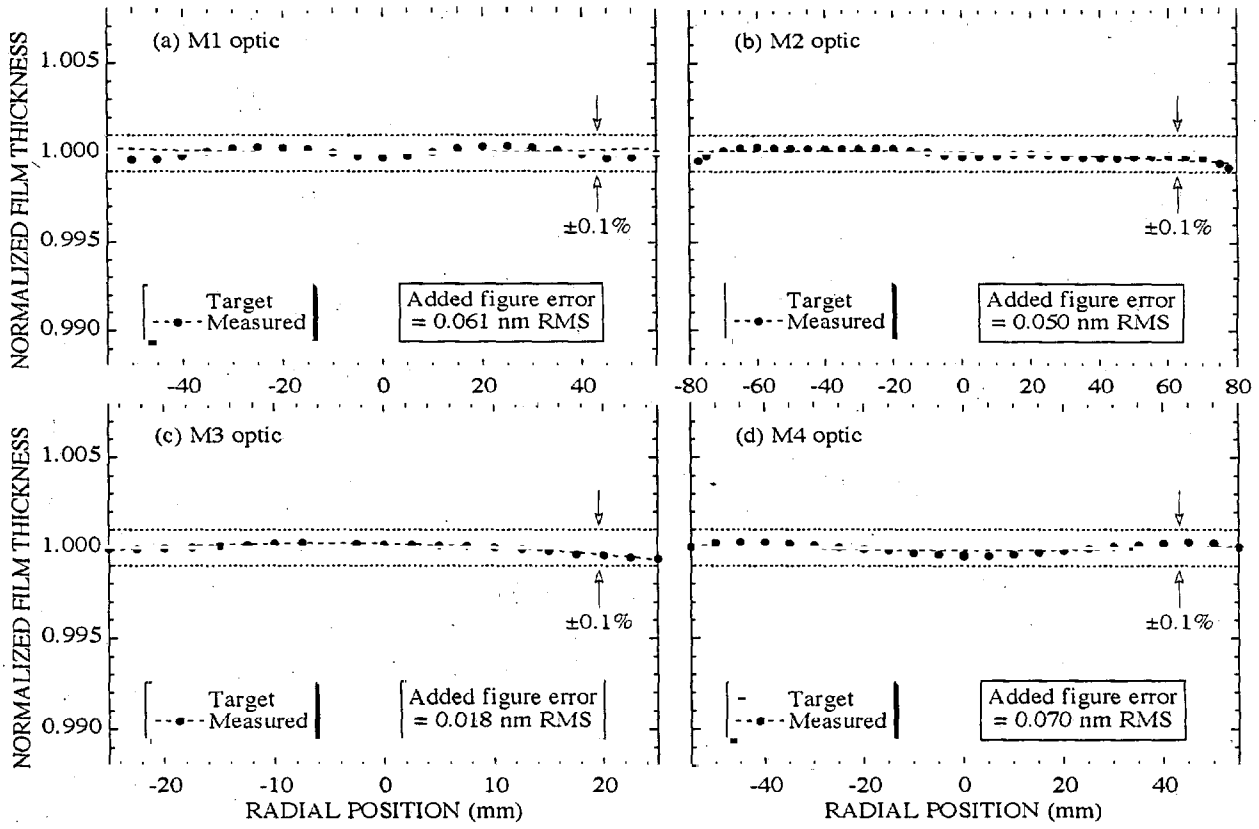

Figure 18. Normalized thickness distribution of all four projection optics. The solid circles are the measured values, the solid line is the targeted thickness profile, the dotted lines are the boundaries of the ±0.1% tolerance zone, and the dashed lines are second degree polynomial fits to the measured data points.

The condenser optics require multilayer coatings with a thickness gradient to accommodate a variation in ray angles across the optic. The thickness control tolerance across the large (260 mm diameter) deeply concave C1 optic and the small C3 optics was ±0.4%. Two full sets of six C1 optic elements and two full sets of six C3 optics plus few spares were coated.[17] Figure 19 (a) and (b) show the average normalized thickness profiles for six C1 and ten C3 elements, respectively. (Note: there were two multilayer designs for the C3 elements, one optimized for an incident angle of 10.645° and the other optimized for 11.850°. Only the results of the 10.645°-design are shown here. The results for the 11.850°-design are very similar). The thickness distribution lies within a ±0.25% zone, well within the specified ±0.4% tolerance zone. For the six C1 elements, the average peak reflectance was 66.4%, and the peak position (centroid) was 13.29 nm at all radial positions between 55 mm and 130 mm. For the C3 elements, the average peak position (centroid) value was 13.277 nm and 13.291 nm for the 11.850°- and 10.645°-design, respectively, with an average reflectance of 66%.

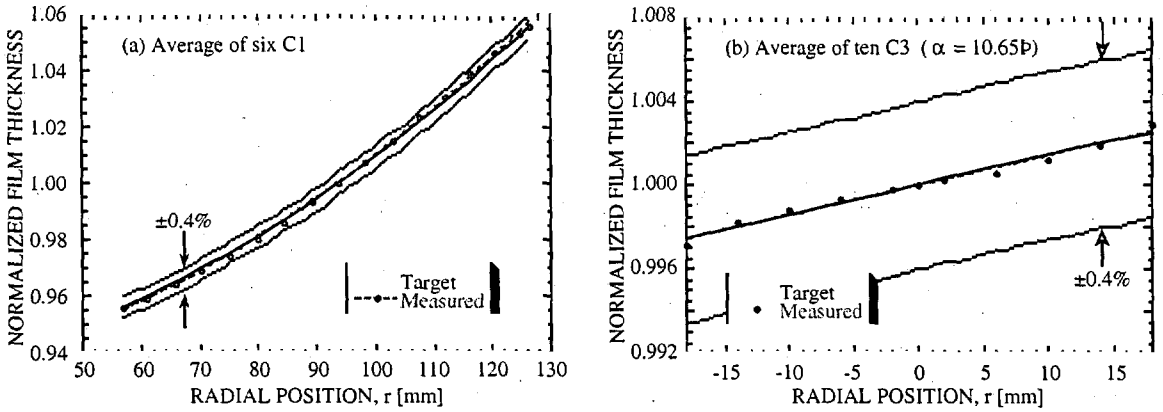

Figure 19. Average normalized thickness profiles for (a) a set of six C1 elements and (b) ten C3 optical elements to be used at 10.645°. The circles are the measured values, the solid lines are the targeted thickness profile, the dashed curves are second degree polynomial fits to the measured points, and the dotted lines represent the boundaries of ±0.4% tolerance zones.

Run-to-run repeatability of deposition rate is critical to insure that all optics in a system reflect at the same peak wavelength. Wavelength-mismatched optics reduce the optical throughput of a system with multiple reflections. Since our deposition system could coat only one optic at a time because of size limitations, run-to-run repeatability of thickness had to be controlled to within 0.4%. Figure 20 (a) shows the reflectance versus wavelength curves for all six condenser and projection optics together.. The wavelength shifts among the curves are relatively small compared to the spectral width of the reflectance peak. Figure 20 (b) shows the product of all six measured reflectance curves (solid line) together with a calculated product curve assuming perfect wavelength matching (dashed line). The area under the measured product curve fills 96% of the area under the perfect-match product curve, i.e., only 4% of the throughput of the optical system was lost because of imperfect wavelength matching. This loss of throughput is well within the 15% mismatch loss budgeted for the ETS optics.

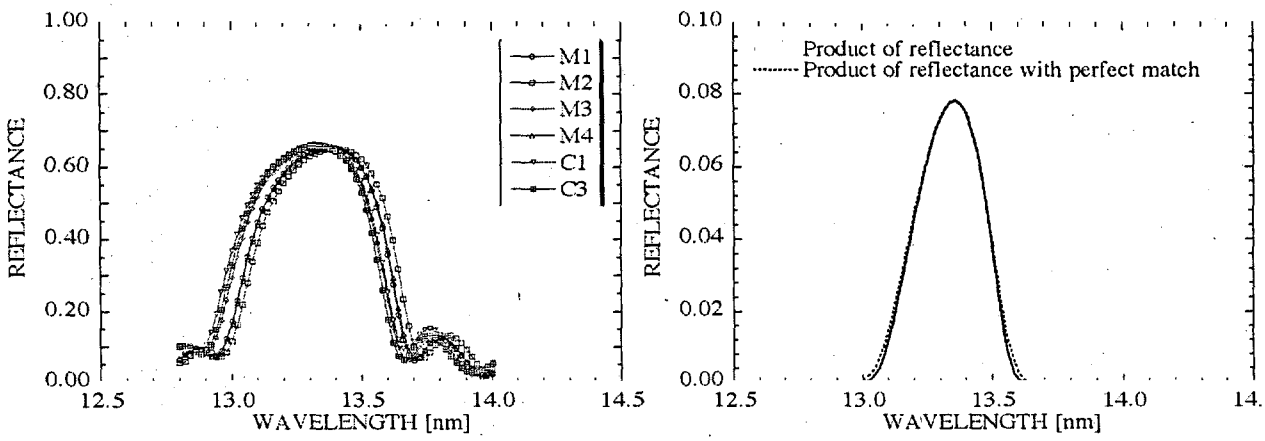

Figure 20. (a) Representative reflectance versus wavelength curves for each of the six condenser and projection optics. (b) Product of the measured reflectance curves shown in (a) together with the calculated product curve assuming perfect wavelength matching.

9. SUMMARY

The EUV ETS is in the subsystem testing phase. The projection system has been aligned and characterized using the development (set 1) optics, while the final ETS optics (set 2) are in an advanced stage of fabrication. Multilayer coatings on both projection and condensing systems meet or exceed specifications for uniformity and wavelength matching. The drive laser has demonstrated performance meeting or exceeding all ETS specifications and continues to perform at that level after approximately one year of operation. The ETS illuminator has been assembled, aligned and characterized at EUV wavelengths using a low power laser, achieving a pupil fill in close agreement with the design. Environmental data is being

acquired using the ETS illuminator, in which the gas-blend system has been installed. Developmental maglev scanning stages have demonstrated stage synchronization jitter and mean position error better than ETS specification. Vacuum-compatible ETS stages are in fabrication and near completion.

ACKNOWLEDGMENTS

The authors are indebted to the members of the subsystem teams and technology teams, whose hard work is responsible for advancing the EUV Engineering Test Stand to the state of development reported in this paper.

This work was performed under the auspices of the U.S. Department of Energy by the University of California Lawrence Livermore National Laboratory under Contract No. W-7405-ENG-48 and Sandia National Laboratories under Contract No. DE-AC04-94AL85000. Funding was provided by the Extreme Ultraviolet Limited Liability Corporation under a Cooperative Research and Development Agreement.

REFERENCES

1. C. Montcalm, S. Bajt, P. B. Mirkarimi, E. Spiller, F. J. Weber, and J. A. Folta, "Multilayer reflective coatings for extreme-ultraviolet lithography," in *Emerging Lithographic Technologies II*, Y. Vladimirsky, Ed., Proceedings of SPIE Vol. 3331, 42-51 (1998).
2. J. E. M. Goldsmith, K. W. Berger, D. R. Bozman, G. F. Cardinale, D. R. Folk, C. C. Henderson, D. J. O'Connell, A. K. Ray-Chaudhuri, K. D. Stewart, D. A. Tichenor, H. N. Chapman, R. Gaughan, R. M. Hudyma, C. Montcalm, E. A. Spiller, J. S. Taylor, J. D. Williams, K.. A. Goldberg, E. M. Gullikson, P. Naulleau, and J. L. Cobb, "Sub-100-nm Imaging with an EUV 10x Microstepper," in *Emerging Lithographic Technologies III*, Yuli Vladimirsky, Editor, Proceedings of SPIE Vol. 3676, pp. 264-271 (1999).
3. G. D. Kubiak, L. J. Bernardez, K. Krenz, W. C. Replogle, W. C. Sweatt, D. W. Sweeney, R. M. Hudyma, and H. Shields, "High-power source and illumination system for extreme ultraviolet lithography," Proceedings of the SPIE vol. 3767, 136 (1999).
4. G. D. Kubiak, L. J. Bernardez, K. Krenz, and W. C. Sweatt, "Scale-up of a cluster jet laser plasma source for extreme ultraviolet lithography", Proceedings of the SPIE vol. 3676, 669 (1999).
5. D. W. Sweeney, R. Hudyma, H. N. Chapman, and D. Shafer, "EUV optical design for a 100 nm CD imaging system," Proceedings of SPIE 3331 2–10 (1998).
6. R. M. Hudyma, H. N. Chapman, D. W. Sweeney, and D. R. Shafer, "Reflective optical imaging system with balanced distortion," US patent 5,973,826 (1999).
7. G. E. Sommargren, in *OSA Trends in Optics and Photonics*, Extreme Ultraviolet Lithography Vol. 4, edited by G. D. Kubiak and D. R. Kania (Optical Society of America, Washington DC), pp. 108–112 (1996).
8. H. N. Chapman and D. W. Sweeney, "A rigorous method for compensation selection and alignment of microlithographic optical systems," Proceedings of SPIE 3331, 102–113 (1998).
9. M.E. Williams, P. Faill, S. P. Tracy, P. Bischoff, and J. Wronosky, "Magnetic Levitation Scanning Stages for Extreme Ultraviolet Lithography", ASPE 14th annual meeting, Monterey CA., November (1999).
10. J. B. Wronosky, T. G. Smith, J. R. Darnold, "Development of a Wafer Positioning System for the Sandia Extreme Ultraviolet Lithography Tool", NASA 3rd International Symposium on Magnetic Suspension Technology, Tallahassee, Fla., December (1995).
11. M.Williams, P. Faill, et.al., "Six Degree of Freedom Mag-Lev Stage Development", Proceedings of the SPIE Conference, March, Vol. 3051 (1997).
12. S.J. Choi, D.J. Rader and A.S. Geller, "Massively parallel simulations of Brownian dynamics particle transport in low pressure parallel-plate reactors," J. Vac. Sci. Tech. A Vol. 14, 660 (1996).
13. J. S. Taylor, G. E. Sommargren, D. W. Sweeney, and R. M. Hudyma, "The fabrication and testing of optics for EUV projection lithography", *Emerging Lithographic Technologies II*, Proceedings of SPIE vol. 3331, pp. 580-590 (1998).
14. G. Campbell, G. E. Sommargren, D. W. Phillion, "Measurement of aspheres using phase shifting diffraction interferometry", paper presented at the OSA Annual Meeting and Exhibit, October 20-24, Rochester, NY (1996).
15. E. M. Gullikson, "Scattering from normal-incidence EUV optics", *Emerging Lithographic Technologies II*, Proceedings of SPIE vol. 3331, pp. 72-80 (1998).
16. D. G. Stearns, R. S. Rosen, and S. P. Vernon, "Fabrication of high-reflectance Mo-Si multilayer mirrors by planar-magnetron sputtering," J. Vac. Sci. Technology A 9, 2662-2669 (1991).
17. C. Montcalm, R. F. Grabner, R. M. Hudyma, M. A. Schmidt, E. Spiller, C. C. Walton, M. Wedowski, and J. A. Folta, "Multilayer coated optics for an alpha-class extreme ultraviolet lithography system," in *EUV, X-Ray, and Neutron Optics and Sources*, S. P. Vernon and K. Goldberg, Eds. Proceedings of SPIE Vol. 3767, 210-216 (1999).